Materials & Design 256 (2025) 114279

Contents lists available at ScienceDirect

Materials & Design

journal homepage: www.elsevier.com/locate/matdes

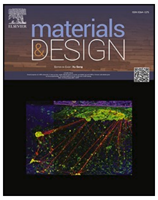

# Automated system for high-throughput process-structure-property dataset generation of structural materials: A $\gamma/\gamma'$ superalloy case study

Thomas Hoefler [*], Ayako Ikeda, Toshio Osada [*], Toru Hara, Kyoko Kawagishi, Takahito Ohmura

*Research Center for Structural Materials, National Institute for Materials Science, NIMS, 1-2-1 Sengen, Tsukuba, Ibaraki, 305-0047, Japan*

ARTICLE INFO

*Keywords:*
High-throughput method
Nanoindentation
Image analysis
$\gamma/\gamma'$ superalloy
Aging heat treatment

## ABSTRACT

We present an automated high-throughput method capable of gathering 2400 data points relating processing conditions, microstructure geometry and yield strength in just 13 days. An estimated 200 times faster than conventional methods using tensile testing specimens, a complete Process-Structure-Property (P-S-P) dataset is created from a single sample. The method is demonstrated by example of the aging heat treatment process of a $\gamma/\gamma'$ superalloy. By aging the sample in a temperature gradient, a wide range of aging process temperatures is mapped over the sample length. Structure analysis consists of fully automated, nanometer-resolution FE-SEM scanning, with precipitate fraction, size and shape distributions determined by automatic image analysis using the Python programming language. Mechanical properties are evaluated by nanoindentation inverse analysis, an approach combining instrumented indentation data with pile-up analysis to calculate stress/strain curves. While the necessary topographic data is typically acquired using atomic force microscopy, a significant speedup was achieved by automatic indent detection and scanning using Angular selective Backscatter FE-SEM analysis. As a method to rapidly assemble comprehensive and consistent P-S-P datasets, we expect it to facilitate efficient alloy design, given a vast majority of modeling approaches still heavily rely on empirical data.

## 1. Introduction

Process-Structure-Property (P-S-P) experimental datasets are a key component for accelerating the development and industrial implementation of structural materials [1–4]. Stimulated by overarching materials research initiatives such as the Materials Genome Initiative [5–7] and the European Materials Modelling Council [8,9], several enterprises focusing on the multi-scale modeling of structural materials have emerged in the last two decades [10,11]. This includes research centers (for example the Center for PRedictive Integrated Structural Materials (PRISMS) [12], the Center for Hierarchical Materials Design (CHiMaD) [13] and the Interdisciplinary Centre for Advanced Materials Simulation (ICAMS) [14]), inter-institutional efforts like the SIP-Materials Integration Projects in Japan [10–15] and venture companies such as QuesTek offering related Software-as-a-Service products [16]. All of them share the vision of accelerating the discovery and development of novel materials.

Structural materials typically feature complex, hierarchical microstructure tailored to meet material specifications for their respective applications [17], requiring both careful alloy design and process optimization. A major challenge in the multi-scale modeling of these materials is the intercorrelation of properties gathered at different length scales and by different instruments [18]. For the industrial implementation of newly designed alloys, understanding of the Process-Structure-Property interrelations is fundamental. In particular, development and optimization of multi-component alloys such as superalloys [19–22] and high entropy alloys [23–27] for high-temperature component applications require a large number of P-S-P datasets. Historically, Ni-base superalloys were designed and gradually improved for new applications using mostly empirical relationships and a limited number of P-S-P datasets through a trial-and-error strategy. Their large number of alloying elements (Ni, Co, Cr, W, Mo, Al, Ti, Ta, Hf, Nb, Re, Ru, C, B, Zr, etc.) [20,21] and complex hierarchical microstructure features [4,7,28–30] controlled by several steps of heat-treatment schedules at a wide range of temperatures and times [31–36] make predictive modeling a formidable task.

While consistently solving inverse problems of computationally designing new superalloys to a meet a given set of material properties

---

[*] Corresponding authors.
*E-mail addresses:* hoefler.thomas@nims.go.jp (T. Hoefler), osada.toshio@nims.go.jp (T. Osada).

https://doi.org/10.1016/j.matdes.2025.114279
Received 13 February 2025; Received in revised form 25 April 2025; Accepted 19 June 2025

without any trial and error is still unfeasible [10], calculations can serve as a starting point [37] for identifying promising candidates or help incrementally improve on existing designs. So far, programs aiming to aid alloy design relying heavily on experimentally gathered P-S-P datasets [22,38,39,40] demonstrated to be helpful for alloy development and practical implementation. Phase diagram calculations [41] (CALPHAD) using thermodynamic and kinetic databases [42,43] can help predict equilibrium phase compositions and diffusion kinetics (which are critical for both heat treatment and mechanical properties at high temperature), and are thus widely used for process and microstructure optimization. While the necessary formulations for the Gibbs free energy of the phases involved can be theoretically derived from density functional theory (DFT) calculations, accurate databases for CALPHAD still heavily rely on experimental data [44–48] in the form of Process-Structure relationships. DFT calculations have also given insight into fault energy estimation, such as antiphase boundary and stacking fault energies [49,50], and the emergence of machine-learning methods has also resulted in some initial applications to superalloy design [36,51,52]. However, without experimental datasets, it remains difficult to predict even the yield strength of advanced alloys incorporating complicated microstructures. Thus, there still is an urgent need for experimental investigation. Databases are still lacking over a wide range of unexplored compositions, leading to high variability depending on choice of database. Although recent text data mining techniques are expected to be helpful for collecting large numbers of existing experimental datasets from open/published papers and reports [53–58], data inconsistencies caused by differing methods, equipment, institutions and researchers could pose a problem when trying to assemble P-S-P datasets in this way. Therefore, to this date, beyond simpler model alloys, simulation programs produce unreliable results for more complex systems such as typical, commercial alloys in practical use.

This has led to the emergence of high-throughput analysis methods, which typically attempt to accelerate the otherwise laborious process of gathering single data points by micro- or nanoscale analysis of gradient samples. Examples pertaining to superalloys include the determination of phase stability across a wide range of compositions (typically of undesirable phases such as TCP) (P-S interrelation) [59–62], determination of multi-element interdiffusion coefficients for creep property prediction (P-S-P interrelation) [63], automatic image analysis of $\gamma'$ precipitate fraction, size and morphology to predict precipitate coarsening depending on single-element additions to a multi-component alloy by using neural networks (P-S interrelation) [64], investigation of the oxidation resistance, elastic modulus/hardness and microstructure of a composition-graded Ni-superalloy (P-S-P interrelation) [62], temperature-graded solution treatment for phase stability, microstructure and Vickers hardness analysis (P-S-P interrelation) [65], nanoindentation hardness, EPMA compositional and SEM microstructural screening of a high-entropy superalloy diffusion couple (P-S-P interrelation) [66] and determination of orientation- and composition-dependent stress–strain-curves calculated from nanoindentation results using a diffusion couple (P-S-P interrelation) [67]. While especially widespread access to automatic image analysis libraries as well as segmentation techniques using artificial intelligence [68] have helped reduce the burden of data analysis, data acquisition is to a large part still performed manually, e.g. framing and focusing SEM or EPMA scans.

We propose an automated high-throughput evaluation system for rapid acquisition of a P-S-P dataset, interrelating the processing parameters, microstructure features and resulting properties. To demonstrate feasibility of the method, we will use a $\gamma/\gamma'$ superalloy with an aging process (P), automatically evaluate $\gamma'$ phase fraction, size and shape from the as-aged structure (S) and gather hardness and stress/strain mechanical properties (P) by combining nanoindentation and scanning electron microscopy (SEM). A single-crystal Ni-Co base superalloy sample undergoing an aging treatment in a gradient temperature furnace is fully automatically sampled at 2400 positions, allowing measurements over all relevant temperatures. Core part of the method is acquisition of all data at equal positions, allowing direct P-S-P correlation.

## 2. Materials and methods

### 2.1. Workflow for high-throughput automated evaluation

Fig. 1 shows the analysis workflow for the high-throughput method used in this paper. A temperature gradient furnace imparts aging heat treatment over a continuous range of aging temperatures on a sample. The sample then undergoes nanoindentation testing and SEM analysis, using sampling coordinates spanning the whole length of the sample. This combination of a gradient heat treatment process with fast micro/nanoscale analysis methods and fully automatic data processing allows building a whole P-S-P dataset correlating the Process (aging temperature and time), Structure (volume fraction, size distribution and shape of $\gamma'$ precipitates) and Properties (hardness and stress–strain curves) from a single sample in a matter of days. Details of the method will be outlined below.

### 2.2. Materials and gradient furnace heat-treatment

A single-crystal sample of Ni-Co base superalloy TMP-5002 for turbine disk applications designed at NIMS and Honda R&D was used in the present work [69]. While intended for use as a polycrystalline turbine disk alloy using multi-step heat treatments, a single-crystal sample with just one aging treatment is used for demonstration of the method. Nominal and actual compositions are shown in Table 1. Grain boundary strengthening elements (C, B, Zr) were excluded from the original composition. Single-crystal round bars of diameter 13 mm × length 130 mm were cast, then screened for stray crystals by complete surface polishing up to grit size 1000 following macro etching. Further, crystal orientation was evaluated using Laue X-ray backscattering diffraction. Next, the samples were quartz encapsulated under Argon gas and homogenized at 1200 °C for 100 h, followed by water quenching in a few tens of liters of unagitated room temperature water. Finally, the diameter 5.8 mm × length 80 mm specimen for gradient aging treatment was cut from one of the round bars using electric discharge machining (EDM).

The experimental setup for the thermally graded aging heat treatment is depicted in Fig. 2a. The same apparatus was also used in a recent work on optimizing the heat treatment temperature of thermoelectric materials by Yurishima et al. [70]. The single-crystal sample is placed inside an alumina tube, which is then lowered into the vertical carbon furnace tube. A one-end-closed quartz glass tube maintained atmospheric control, with constant Ar gas flow kept during the experiment. With an infrared heating heater placed at the top end and a water cooling jacket at the lower end of the heated zone, a temperature gradient is imposed upon the sample. The temperature across the sample is determined by a prior calibration from measuring the unloaded furnace with a trailing type R thermocouple inserted from the bottom of the furnace, the results of which are shown in Fig. 2b. Interpolation between the measured points is performed using cubic splines, allowing calculation of the temperature at any position of the sample. The range of the temperature gradient on the sample can be controlled both by the (constant) setpoint temperature of the furnace and the vertical location of the sample in the carbon pipe by using carbon spacers inserted below the sample assembly.

For the present work, the sample was placed inside the cold furnace at 59–139 mm from the top cap, the resulting temperature gradient ranges from 1208–647 °C (cf. the hatched region in Fig. 2b). The achievable heating rate was limited by the carbon tube inside the furnace, requiring a linear 30 min heating ramp to ensure that the sample is heated at the target rate. After heating, the furnace setpoint temperature was held constant for three hours, resulting in a steady-state temperature gradient profile across the sample. Finally, the

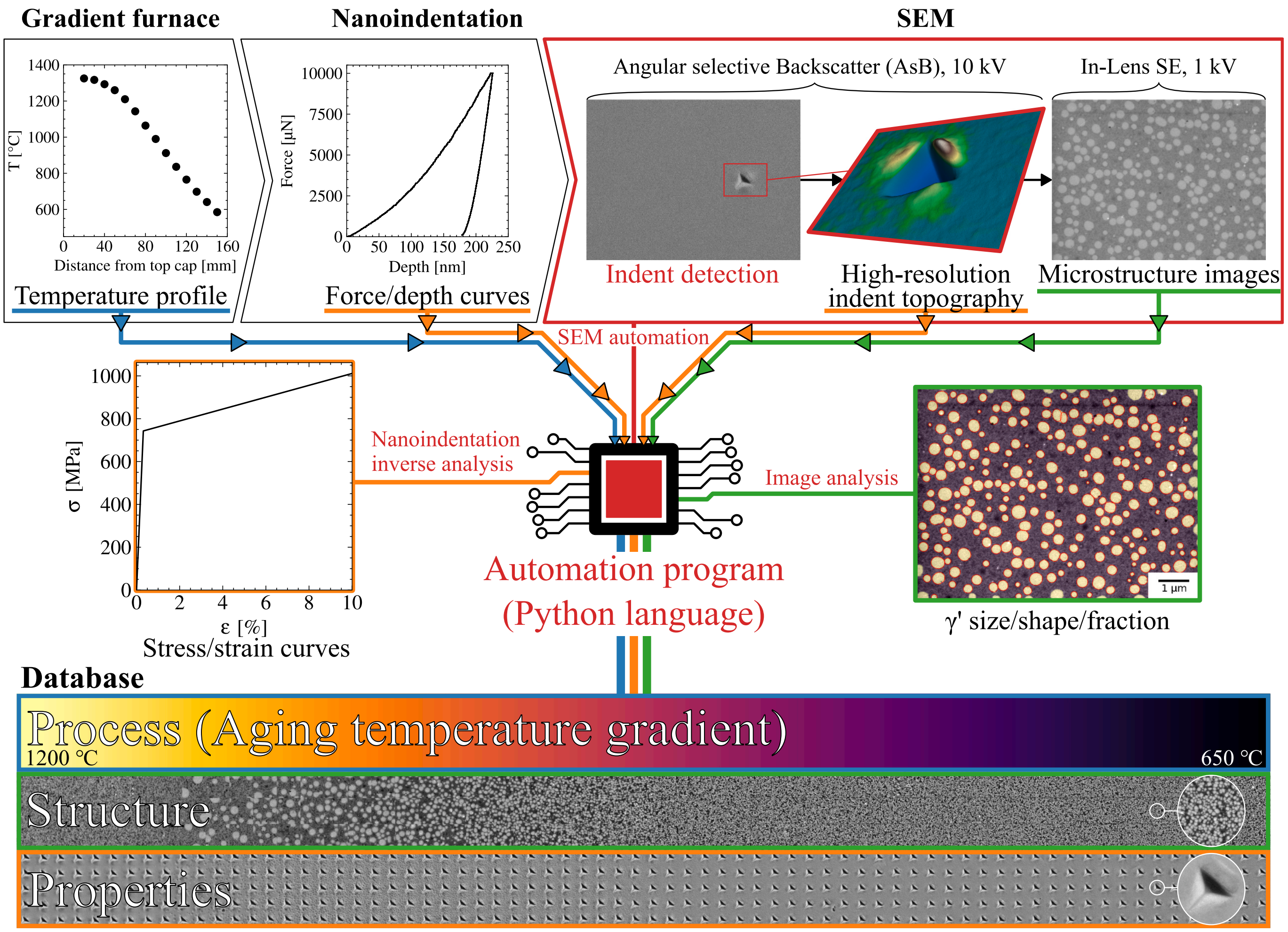

**Fig. 1.** High-throughput analysis workflow and data acquired. Aging temperature, force/depth curves, indent topography as well as γ′ area fraction, particle shape and size distributions are gathered for a temperature gradient-aged sample by automatic image analysis and nanoindentation inverse analysis using automated nanoindentation and SEM measurements. The automation program developed for this method manages measurement, processing and storage of data, generating the P-S-P database correlating the Process (aging), Structure (γ′ size/shape/fraction) and Properties (hardness, stress/strain curves).

**Table 1**

Composition by mass for Ni-Co superalloy TMP-5002 used in the present study. Actual composition was determined by ICP-AES.

| | Cr | Co | Mo | W | Ti | Al | Ta | Hf | Nb | Ni |
|---|---|---|---|---|---|---|---|---|---|---|
| Nominal | 11.7 | 27.0 | 3.4 | 1.9 | 4.4 | 3.2 | 2.2 | 0.35 | 0.5 | Bal. |
| Actual | 11.4 | 26.6 | 3.38 | 1.90 | 4.35 | 3.07 | 2.18 | 0.33 | 0.48 | Bal. |

sample was quenched by dropping into an unagitated water bath placed beneath the furnace, containing a few tens of liters of room temperature water. After the aging heat treatment, the sample was split longitudinally across the (100) plane using EDM, where <001> is defined to be the crystal direction closest to the height (axial direction) of the round bar sample. To facilitate polishing, the resulting halves were sectioned to 43 mm length as to cover the whole gradient (length 80 mm) with an overlap region of 6 mm length. The resulting specimens were then wax-mounted, ground, polished and finally vibratory polished in 30 nm colloidal silica suspension.

### 2.3. Nanoindentation and microstructure observation

Following preparation, the sample underwent room temperature nanoindentation testing, using a Bruker Hysitron TI 950 TriboIndenter. Testing was load-controlled with a maximum force of 10 mN, 10 s holding time and loading/unloading rate of 2 mN/s. For each of the two sample halves, a grid of 120 × 10 indents over an area of 42000 μm × 300 μm (spacing 353 μm and 33 μm) was performed using automated testing. 20 of the indent columns at equal temperature were performed in the overlap region between the samples, resulting in a total of 2400 indents at 220 different aging temperatures.

Next, microstructure and indent topography were automatically analyzed at all 2400 positions using FE-SEM (Zeiss GeminiSEM 300) with the automation program developed for this high-throughput method. As preparation for the automatic scanning routine, sample insertion, beam adjustment, and location of the indent pattern were performed manually. Next, the automation program performed fine rotation correction by querying the operator to center on some of the indents, reading the resulting coordinates in order to set the scan rotation to correctly align the indent pattern. To account for changing working distance due to minute differences in the sample surface height, a focus plane was generated using a Clough-Tocher interpolation scheme, with the program automatically moving to a few of the indent

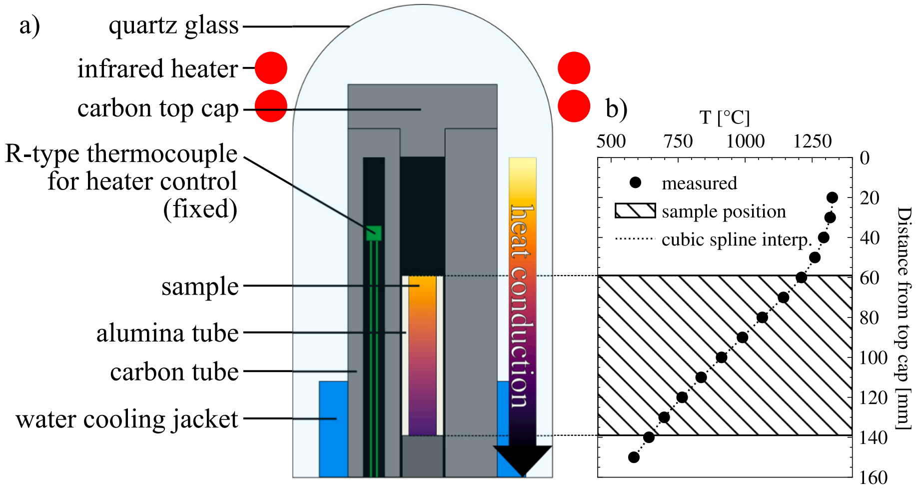

**Fig. 2.** Gradient furnace for aging heat treatment of high-throughput samples. a) Schematic of the essential parts of the gradient furnace, loaded with the sample b) Temperature profile inside the carbon pipe as measured inside the unloaded carbon tube by a trailing type R thermocouple before the experiment, with the hatched area depicting the sample position during the experiment.

locations and querying the operator to adjust focus and stigma correction. After this initial setup phase, all indent locations were known up to an error of about 2–3 μm (mostly limited by the accuracy of the SEM stage motor and indenter offset), together with the necessary focusing parameters. Automatic scanning then proceeded in three steps for each indent location, as outlined in the upper right SEM section in Fig. 1: Indent identification at low magnification to correct for positioning errors, high magnification scanning with the indent centered in frame using beam shift, and microstructure imaging within a few μm distance of the indent. Each of these three steps will be described in detail below.

First, the exact indent location was determined by a wide-field scan, with the scan window height set to ten times the indent side length expected from the indent depth, known from the indentation testing results. Imaging was performed using the Angular selective Backscatter (AsB) detector at 10 kV acceleration voltage, with the four annular detector quadrants scanned simultaneously using the four detector channels available (typically termed “Quad mode”). Given the four images at differing detector angles, topographic information was calculated by integration using the automation program. The resulting topographic map was then sampled for local height minima, with an absolute threshold set at the median height minus a wavelet-based estimate of the signal noise. Out of these minima, which sometimes included contaminants or porosity, indents were identified by flood-filling from the minimum up to two thirds the distance to the median height and fitting a triangle to the convex hull of the resulting mask. Comparison by shape of the fitted triangle with the flood-fill convex hull as well as differences of the internal angles allowed elimination of any false-positives. In cases where more than one indent remained inside the scanned region, the one closest to the expected coordinates was chosen for analysis.

Second, the indent was centered exactly in the scan region using beam shift and the magnification adjusted so that the expected indent side length is equal to half the scan area height, ensuring that all indents were fully in frame and of equal apparent size for all locations. Using the same imaging parameters as in the low magnification step above, topographic information was gathered for the purpose of pile-up determination, which was necessary for the calculation of stress–strain curves from the indentation results via inverse analysis.

In the third and final step of the automatic SEM scanning routine, microstructure images several micrometers close to the indent locations were collected. With the indents out of view, $\gamma'$ area fraction and precipitate sizes at corresponding locations could be acquired for relation to the aging temperature as well as the mechanical property data gathered in the previous steps. The phase contrast between $\gamma$ and $\gamma'$ using the AsB detector was too low for evaluation, requiring imaging using the In-Lens SE detector at a significantly lower acceleration voltage of 1 kV to capture even the fine cooling $\gamma'$ formed during water quenching. Since a change in acceleration voltage entails a wait time of a few seconds for the voltage to stabilize and a need for re-adjustment of focus and alignment, microstructure imaging was performed after all indents were scanned.

During the automatic scanning routines, automatic focusing fine adjustment was performed every ten minutes to account for focus drift, such as caused by thermal expansion of the sample during beam illumination. Furthermore, automatic contrast adjustment was performed during microstructure imaging. All images were acquired using a resolution of 1024 × 768 pixels, including the individual AsB channel images.

## *2.4. Automated dataset generation system*

### *2.4.1. Process dataset*

A sample coordinate space was built from the sample edge points as measured during SEM imaging. In combination with the coordinates gathered at all 2400 sampled locations, the exact position of each point in the gradient furnace during the aging process could be determined. Using the cubic spline interpolation built from the furnace temperatures measured before the aging experiment (see Fig. 2), the corresponding aging temperatures were determined and assembled into the Process dataset. The aging time was a constant 3 h at all positions.

### *2.4.2. Structure dataset*

The Structure (volume fraction, shape and size distribution of $\gamma'$ precipitates) dataset was built from the SEM microstructure images, which were automatically evaluated using the automation program developed in the Python programming language, with the majority of image processing performed using the OpenCV [71] and scikit-image [72] libraries. The processing chain consists of denoising, sharpening, histogram equalization, top-hat transformation, thresholding and finally distance transform-based watershed segmentation to identify the individual $\gamma'$ precipitates. Precipitates with an area of less than 64 pixels were eliminated to prevent noise as well as any cooling $\gamma'$ from affecting the results gathered for the aging $\gamma'$, while average-sized aging $\gamma'$ had an approximate area of 700 pixels at all temperatures due to magnification scaling. For the contour of each identified precipitate, a superelliptical fit was performed, given by Equation 1 [73]. Able to describe shapes between an ellipse (for $n = 2$) and a rectangle (for $n \to \infty$), the fit allows automatic evaluation of shape via the parameter $n$ as follows:

$$r(\theta) = \left( \left| \frac{\cos\theta}{a} \right|^n + \left| \frac{\sin\theta}{b} \right|^n \right)^{-\frac{1}{n}} \tag{1}$$

where $\theta$ is the polar angle; $r(\theta)$ is the radius; $a$ is the semi-major axis; $b$ is the semi-minor axis and $n$ a positive real shape parameter. Thus, $\gamma'$ area fraction, as well as the distributions for equivalent precipitate diameter and precipitate shape were gathered automatically.

Microstructure data gathered from cross sections is necessarily two-dimensional in nature. For the spherical $\gamma'$ precipitates in the present work, area fractions of random sections and volume fractions are equivalent, while apparent diameters gathered from SEM images are different from the actual diameter of the three-dimensional precipitates.

One commonly used method to correct for this and calculate actual precipitate diameter distributions from the apparent size distributions is the Saltykov method [74–76]. However, this method is susceptible to systematic sampling errors such as oversight of small precipitates due to limitations in instrument or scanning resolution as well as sample preparation artifacts [77,78]. These errors will affect the whole range of precipitate sizes considered and can further cause unphysical artifacts such as negative bin frequencies.

Instead, we fitted the theoretically expected apparent precipitate size distribution to experimental data, from which we could then gather the actual, three-dimensional mean precipitate diameter. We used the Lifshitz-Slyozov encounter modifed (LSEM) theory to model both the precipitate size distribution and the coarsening rate during the aging process, which extends upon the LSW theory to account for precipitate coalescence at non-zero volume fractions [79–82]. The apparent cumulative size distribution for random plane sections $F(d_\mathrm{A})$ was calculated as described by Takahashi and Suito [78] (Eq. (2)), where $d_\mathrm{A}$ is the apparent diameter, $d_\mathrm{V}$ the actual precipitate diameter, $f(d_\mathrm{V})$ the actual precipitate diameter probability density function (PDF), and $\mu_{d_\mathrm{V}}$ the mean precipitate diameter. The apparent size PDF was then calculated by numerical derivation and fit to experimental distributions, which were gathered from the observed precipitate apparent diameters by gaussian kernel density estimation.

$$F(d_A) = 1 - \frac{\int_{d_\mathrm{A}}^{\infty} \sqrt{d_\mathrm{V}^2 - d_\mathrm{A}^2} f(d_\mathrm{V}) \mathrm{d}(d_\mathrm{V})}{\mu_{d_\mathrm{V}}} \tag{2}$$

### 2.4.3. Properties dataset

The Properties dataset containing hardness and stress–strain curves was generated by nanoindentation inverse analysis correlating the multiaxial deformation during nanoindentation with the uniaxial tensile deformation of a polycrystalline sample with randomly oriented cubic crystal grains, as previously proposed by Goto et al. [67,83,84]. In the present work, by using four-channel AsB SEM scanning instead of AFM (atomic force microscopy) to gather the necessary topographic information as in the original method by Goto et al., a significant speed-up could be achieved.

First, the topographic information gathered by SEM is tilt-corrected and normalized by using the final indent depth as determined during indentation testing. The normalized pile-up height $H_p$ is calculated according to Equation 3, where $h_\mathrm{max}$ is the maximum indent depth and $h_{p(k)}$ is the maximum pileup height on the three lines $k$ going from the indent corners through the indent center. Assuming linear strain hardening, $\sigma_y = \frac{A}{\left(1-\frac{B}{E}\right)}$ with slope $B$ and intercept $A$ and assuming proportionality of nanoindentation hardness $H$ to a representative stress $\sigma_r = \frac{H}{k_e} = A + B\varepsilon_r$ at strain $\varepsilon_r$, stress–strain curves can be calculated from the nanoindentation results using the relation shown in Equation 4. The parameters used are shown in Table 2. All calculations were performed using the reduced Young's modulus $E_\mathrm{r}$, which is related to the sample's Young's modulus $E$ by $\frac{1}{E_\mathrm{r}} = \frac{1-{\nu_\mathrm{i}}^2}{E_\mathrm{i}} + \frac{1-\nu^2}{E}$, where $E_\mathrm{i}$ and $\nu_\mathrm{i}$ are the Young's modulus and Poisson's ratio of the indenter, and $E$ and $\nu$ the Young's modulus and Poisson's ratio of the sample.

**Table 2**
Parameters used in the indent inverse analysis [67].

| $\varepsilon_r$ | $k_e$ | $k_{p1}$ | $k_{p2}$ | $k_{p3}$ |
|---|---|---|---|---|
| 0.08 | 7.23 | 1 | 0 | 229.1 |

$$H_p = \frac{\sum_{k=1}^{3} h_{p(k)}}{3\, h_\mathrm{max}} \tag{3}$$

$$H_p = k_{p1} exp\left( -\frac{k_{p2}\sigma_y + k_{p3}B}{E} \right) \tag{4}$$

## 3. Results

### 3.1. SEM microstructure analysis

The initial microstructure as water-quenched after homogenization was observed as an unimodal distribution of $\gamma'$ particles with a mean diameter of approximately 58 nm. Despite water cooling, nearly full precipitation up to the equilibrium volume fraction was observed. Water quenching was relatively slow due to the quartz encapsulation used during homogenization hindering initial quenching and the lack of water agitation. Further, the core 5.8 mm part of the initial 13 mm homogenized rod was used, resulting in reduced cooling rates while mitigating the effects of uneven contact with the coolant medium. While precipitation of 50 % of $\gamma'$ during water quenching is unusual and surprising, similarly rapid nucleation and growth have been reported for other superalloys under water cooling conditions [85–88].

Results from the automatic microstructure imaging of the temperature gradient-aged sample are shown in Fig. 3. Images are presented in order of decreasing aging temperature, showing the different aging $\gamma'$ morphologies. Magnification is scaled roughly according to the mean apparent diameter of the precipitates. With images acquired with a pitch of 353 μm along the temperature gradient, a mean temperature resolution of 2.6 °C (max. spacing: 3.2 °C) was achieved, while the temperature differences within the sampled regions were within 0.05 °C (e.g. between the high/low temperature facing edges of the SEM images, see Fig. 3b).

No aging $\gamma'$ was observed at 1164 °C and above, which was thus identified as the solvus temperature. Fig. 3a shows an example of the corresponding microstructure, where only fine cooling $\gamma'$ is present. To account for both the lack of aging $\gamma'$ and show the significant amount of cooling $\gamma'$ formed during water quenching, a high-magnification outcrop is overlaid over an image scanned at lower magnification. Under the imaging conditions used, the $\gamma'$ phase appears as light gray as compared to the darker $\gamma$ matrix phase. In contrast to Fig. 3a, at just 2 °C lower, a small fraction of large aging $\gamma'$ was observed at 1162 °C (Fig. 3b). With decreasing aging temperature, increasing fractions of aging $\gamma'$ of decreasing size were observed up until approximately 850 °C (Fig. 3c–f), below which no significant precipitate growth could be observed for the 3 h aging treatment, remaining close to the as-quenched state (Fig. 3g–h). The magnified outcrop in Fig. 3a and i), depicted at the same scale, shows the equivalent microstructures formed during super-solvus water quenching after aging and homogenization, respectively.

Some precipitates exhibited shapes not explicable by Ostwald ripening alone, such as concave elements or L-shaped precipitates. Such instances, outlined red in Fig. 3, were especially common at intermediate temperatures with high volume fractions but significant amounts of coarsening, such as shown at 850 °C in Fig. 3f. Both lower amounts of $\gamma'$ at aging temperature as well as reduced aging progress decreased the frequency of such odd-shaped precipitates.

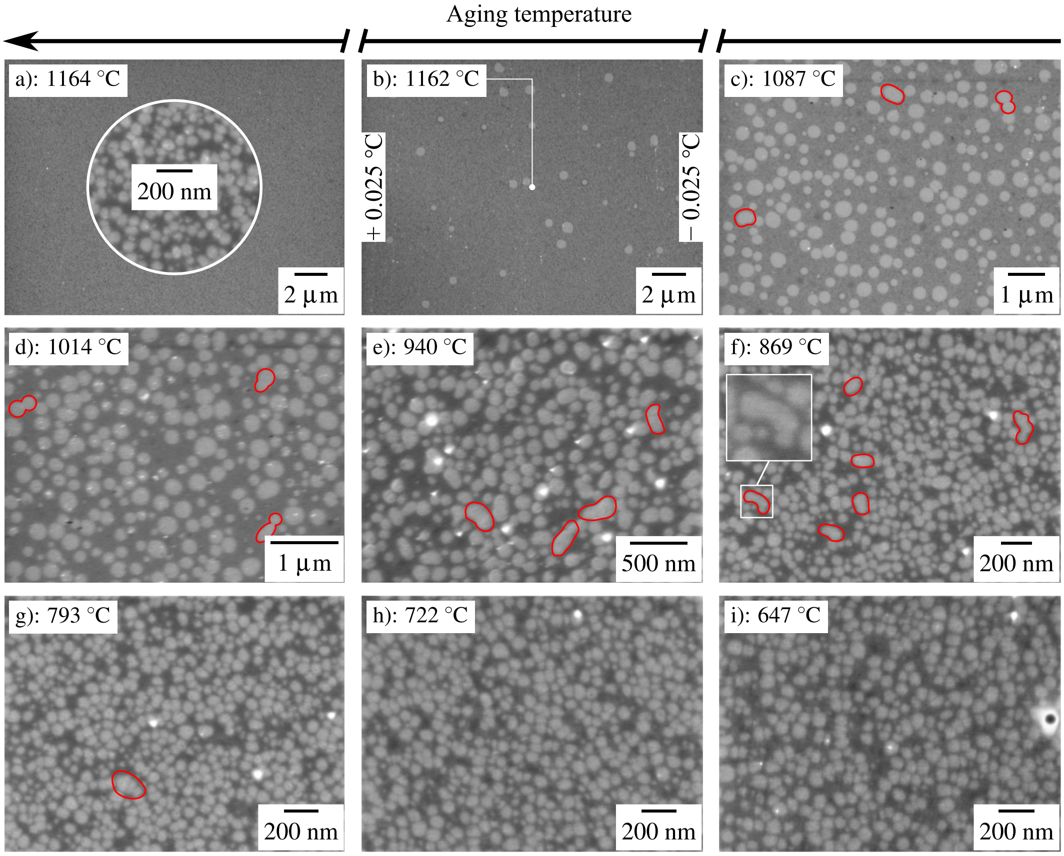

**Fig. 3.** Exemplary microstructure images at different aging temperatures. $\gamma'$ phase appears as a lighter gray embedded inside the darker $\gamma$ matrix. The aging temperature rises from the right to the left, both between and inside each of the images. a) Is just above, and b) just below the solvus temperature. b) Also gives the temperature differential between the high (left) and low temperature (right) edges of the image. Red markings denote examples for odd-shaped precipitates inconsistent with Ostwald ripening, with f) showing a single, magnified example without the marking. Note the differing image scales. (For interpretation of the references to color in this figure legend, the reader is referred to the web version of this article.)

Fig. 4 gives a summary of the microstructure evaluation results. The horizontal axis for aging temperature is shared between all of the plots, giving area fraction, mean apparent diameter from the cross section images and the median value for the shape parameter $n$ of the superellipse fitting according to Eq. (1). Data shown in red signifies aging $\gamma'$, while area fractions determined for cooling $\gamma'$ are marked blue. For each temperature, confidence intervals and mean values are calculated for the 10 measurements at equal temperature. Area fractions (Fig. 4a) of aging $\gamma'$ across the range of aging temperatures observed roughly matches the CALPHAD predictions by Thermo-Calc using the Ni-Data-v8 database (dashed line), although the experimentally observed $\gamma'$ solvus temperature was 1164 °C as opposed to 1181.7 °C by calculation. Accordingly, the CALPHAD calculation overestimates the solvus temperature by nearly 18 °C, or put differently, overestimates the $\gamma'$ volume fraction at the solvus temperature by approximately 5.5 %. Cooling $\gamma'$ was found to fully nucleate and precipitate in the short timeframe during water quenching, which was also observed after homogenization treatment of the samples. Thus, significant fractions of both aging and cooling $\gamma'$ coexist after quenching from temperatures between approximately 950 up to 1162 °C. Quantitative analysis of the precipitate sizes for cooling $\gamma'$ would have required automatic framing of high-magnification SEM scans to exclude the aging precipitates as much as possible, which is currently not implemented in the automatic imaging routine.

The precipitate sizes of aging $\gamma'$, calculated as equivalent diameters from the precipitate areas measured by image evaluation, are depicted in Fig. 4b. Slight fluctuations in mean precipitate diameter can be observed between 650 °C and 750 °C, which is assumed to be caused by imperfections in focus and/or stigma correction at the high magnifications necessary for imaging. Significant growth can be observed for temperatures above about 850 °C. A slight decrease in the slope of the resultant mean diameter over the temperature can be seen starting from about 1050 °C, coinciding with a notable decline in volume fraction.

The precipitate shape, specifically roundness, as evaluated by the superellipse fit according to Equation 1 is shown in Fig. 4c. The shape parameter $n = 2$ describes perfectly round (circular or elliptical) precipitates, while values of $n > 2$ model increasingly cuboidal shapes. As a visual guide, the auxiliary y-axis on the right side of Fig. 4c shows the resulting shapes for the circular case ($a = b$). For alloy TMP-5002, no significant shape transitions during aging were observed, with the sections staying close to the perfectly round shape with $n = 2$ across the whole range of aging temperatures.

Precipitate size distributions for aging $\gamma'$ as determined by automatic SEM image analysis are depicted in Fig. 5. Aging temperatures are depicted color-coded according to the color bar to the right, with lower temperatures in darker, purple tones and high temperatures in yellow. Measurements at equal temperature are aggregated as a single, normalized histogram each, with the resulting frequencies plotted over the automatically calculated bins for the apparent diameter axis. At higher temperatures, significant broadening of the distribution towards larger diameters can be seen. Up to about 940 °C, approximately 5000 precipitate sections are evaluated at each aging temperature, dropping to around 2300 sections at 1060 °C and 1000 sections at 1150 °C as the interparticle distances increase with decreasing volume fractions, resulting in each SEM micrograph containing fewer precipitate sections.

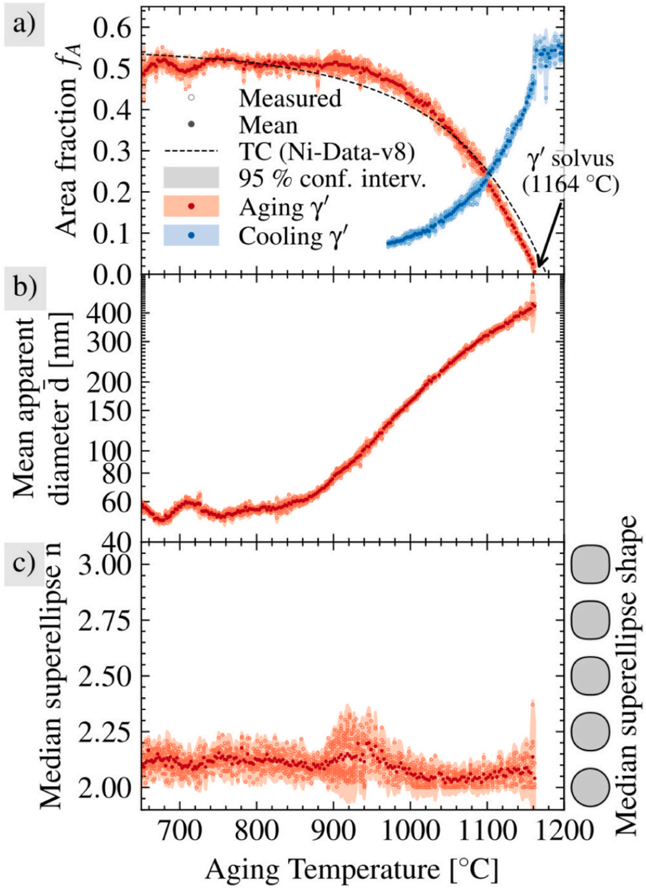

**Fig. 4.** Results of the automatic microstructure evaluation. Results for aging γ′ are shown in red, while cooling γ′ formed during quenching following the gradient aging treatment is shown in blue. A black, dashed line indicates the γ′ phase fraction at aging temperature as calculated by Thermo-Calc using the Ni-Data-v8 database. Note the logarithmic scale on the mean diameter axis. (For interpretation of the references to color in this figure legend, the reader is referred to the web version of this article.)

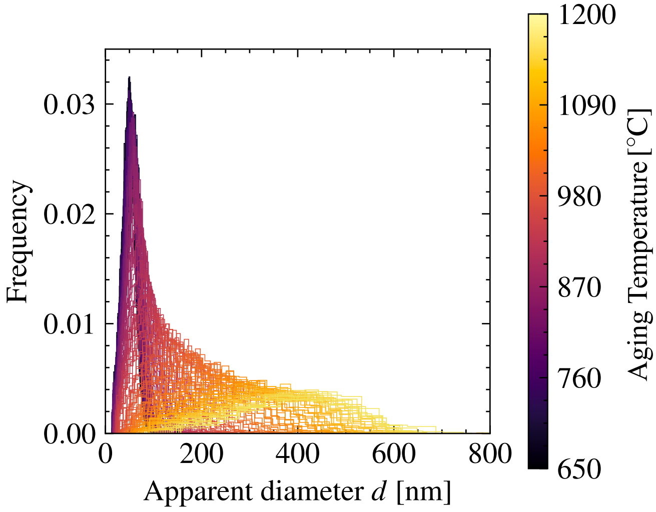

**Fig. 5.** Precipitate size (apparent diameters gathered from SEM cross sections) histograms for aging γ′ at different aging temperatures, which are distinguished by the color scale to the right.

### 3.2. Nanoindentation testing

Fig. 6 shows representative indents as imaged by SEM. Of the four simultaneously acquired quadrant AsB images, only one image each is given for conciseness. Indents are closely similar in appearance at all temperatures, with the smallest shown indent at 647 °C (Fig. 6i) having a side length of 1.36 μm as compared to the largest shown indent at 1014 °C (Fig. 6d) at 1.53 μm. Coarser γ′ precipitates are visible in the surrounding substrate in Fig. 6b–d at 1162 °C, 1087 °C and 1014 °C respectively. Out of the 2400 indents performed, 2382 were automatically located, centered and scanned, resulting in a miss rate of less than 1 %.

The results of the pileup analysis for the indent in Fig. 6i are given in Fig. 7. The four-channel AsB SEM images, together with the final indent depth $h_f$ known from nanoindentation, allow calculation of the height surface shown in Fig. 7a. Pileup is then determined as the local maxima closest to the indent center at the 3 lines passing through each of the corners and the indent center, marked red in the two-dimensional map in Fig. 7b. The height profiles through the center at these angles are given in Fig. 7c, which also gives the mean pileup value $\overline{h}_p$ and the maximum indent depth during indentation testing $h_{\max}$, from which the normalized indent height $H_p$ was then determined as according to Eq. (3).

A compilation of the nanoindentation force/depth curves is given in Fig. 8, with a) showing all data with aging temperature indicated both by color and x axis position, while b) shows results for selected temperatures. The same color scale as in Fig. 5 is used. 54 of the 2400 tests performed were identified as outliers by Grubbs test using the reduced Young's modulus, with 29 of these outliers clustered at approximately 730 °C. As indents at equal aging temperature were performed in sequence before proceeding to the next temperature, it seems likely that temporary tip contamination caused these clustered outliers. The representation in Fig. 8a shows consistent loading and unloading behavior for all aging temperatures, and the change in hardness results in a somewhat sinusoidal shape of the maximum depth datapoints.

Fig. 9 shows the nanoindentation hardness and reduced Young's moduli gathered from the force/depth curves in Fig. 8, together with the pileup ratios determined by SEM analysis, over a shared aging temperature axis. With increasing aging γ′ diameter above approximately 850 °C, a continuous decrease in hardness can be observed up to around 1020 °C in Fig. 9a. Above this temperature, the amount of fine cooling γ′ formed during quenching increases (from 11 % at 1022 °C to 28 % at 1116 °C, and finally 56 % above 1164 °C) while the amount of aging γ′ steadily decreased in accordance to the equilibrium conditions at the respective aging temperature, causing hardness to increase again. The reduced Young's modulus (Fig. 9b) was found to be largely independent of aging temperature and the associated microstructure. The pileup ratio (Fig. 9c) shows a slight downward trend between 950–1150 °C, followed by a slight but sharp increase, showing some correlation to γ′ growth and the solvus temperature of 1164 °C.

## 4. Discussion

### 4.1. Structure: γ′ size distribution and growth rate analysis

The large number of SEM sections acquired at a high temperature resolution inaccessible by traditional methods allows us to perform an in-depth analysis of both the as-aged precipitate size distribution as well as the coarsening kinetics of alloy TMP-5002.

$$d^3 - d_0^3 = 8K(f_V)t \qquad (5)$$

Coarsening of the γ′ phase is modeled using Equation (5), with the diameter $d$ after aging for time $t$ from the initial diameter before aging $d_0$ proportional to the coarsening rate $K$, which is dependent on the volume fraction $f_V$ of the coarsening phase (the constant factor 8 stems from

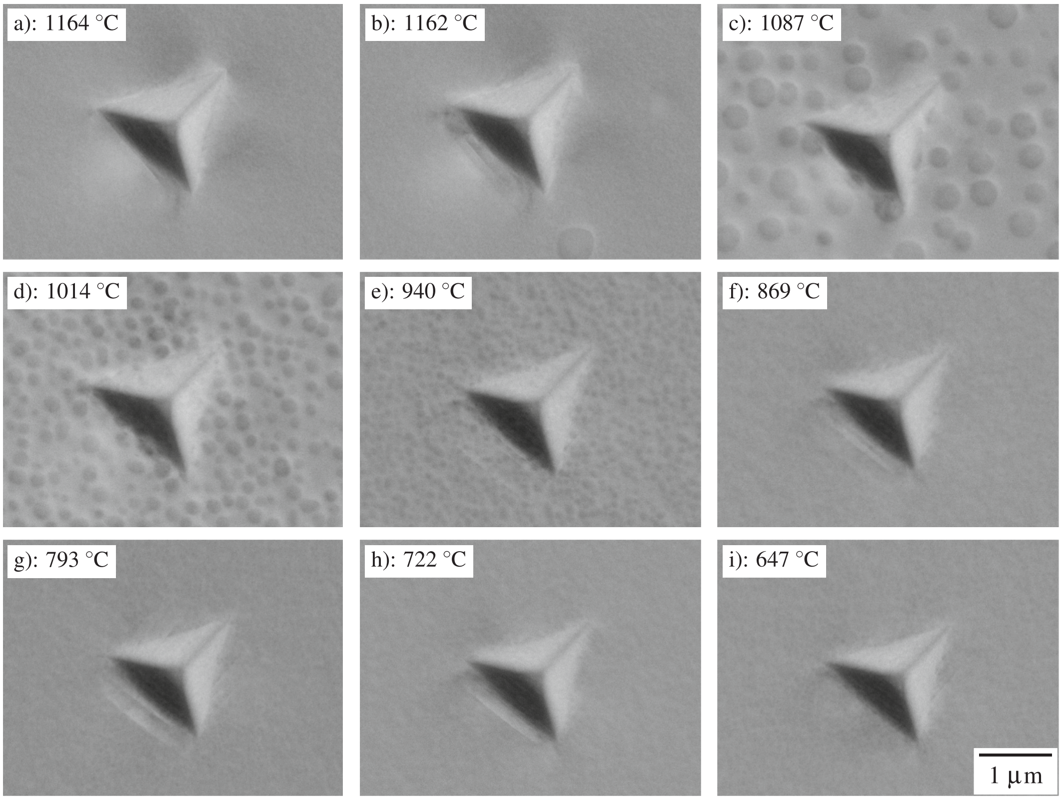

**Fig. 6.** Single quadrant SEM-BSD images at different aging temperatures for room temperature indent pileup analysis. While magnification is automatically scaled according to the apparent indent diameter during analysis, they are shown at equal scale here for size comparison.

using diameters instead of radii). For the present alloy, this dependance on $f_V$ stems from precipitate coalescence, which plays a significant part in the formation of the precipitate sizes observed in Fig. 5. Actual instances of coalesced precipitates were commonly observed in the automated SEM sections, with examples pointed out in Fig. 3. The precipitate size distributions are notably broader than would be expected by LSW theory (which does not take the effects of $f_V$ into account), including diameters beyond the theoretical maximum value of 1.5 times the distribution mean. Furthermore, a drop in the mean apparent diameters in Fig. 4 at temperatures above 1050 °C suggests an influence of the volume fraction at high aging temperatures, which is consistent with coalescence events decreasing in frequency with decreasing volume fractions. To account for these effects, we use the LSEM model originally proposed by Davies et al. [79]. For the simple case of a binary alloy, $K$ can be calculated according to Equation (6) [79,80].

$$K(f_V) = \frac{6\gamma_{IF} V_m c_e \bar{r}^3}{RTY(f_V)} D(T) \tag{6}$$

Where $f_V$ is the volume fraction of the coarsening phase, $\gamma_{IF}$ is the interfacial energy between the two phases, $V_m$ is the molar volume of the coarsening phase, $c_e$ is the equilibrium molar fraction of solute in the matrix phase, $\bar{r}$ is the average radius in the LSEM distribution, R is the universal gas constant, $T$ the temperature, $Y$ (originally termed $\gamma$ by Davies et al.) is a time-independent rate coefficient depending on the volume fraction, and $D$ the diffusion coefficient in the matrix phase. The value of $Y$ also affects the size of the precipitate size distribution, generally leading to broader distributions at higher volume fractions.

Fig. 10a shows the theoretically expected distributions fitted to gaussian kernel density estimates (KDE) using the experimentally observed precipitates as well as the relevant histograms as shown in Fig. 5. Good agreement was found for temperatures above 900 °C, where significant growth occurs within the 3 h aging treatment and the system approaches the asymptotic state. In contrast, there is a larger discrepancy between model and observed values at 647 °C, which corresponds to the initial state after water quenching from the super-solvus homogenization treatment. Precipitate size in this regime is mostly controlled by the dynamic nucleation and growth processes during quenching, with continuously decreasing temperature and increasing volume fraction. To show the effect of volume fraction on the distribution shape more clearly, Fig. 10b depicts the relative size distributions as scaled by the fitted distribution mean value. Lower temperatures with higher amounts of $\gamma'$ phase present during aging exhibit heavier tails towards larger relative sizes and a slight skew to the left when compared to higher temperatures (low volume fractions). The difference between observed and model values at 647 °C is also more apparent here, while the temperatures above 900 °C follow the theoretically expected trend. Fig. 10b further shows the cut-off of smaller particles, which is caused by limitations in image resolution. Given the exclusion of particles with an area of less than 64 pixels and an average-sized precipitate having about 700 pixels area, this results in only particles with approximately 30 % of the mean diameter being detected. Nevertheless, the true mean diameter is recovered by the fitting procedure.

An evaluation of the microstructure results from Fig. 4 according to the LSEM theory of precipitate coarsening, accounting for the effects of precipitate coalescence, is shown in Fig. 11. For the present, multi-element alloy TMP-5002 examined, the equilibrium phase compositions, molar volume, $\gamma/\gamma'$ interfacial energy and diffusion coefficients required for determination of the rate constant $K$ (Eq. (6)) are practically unknown. However, we can perform a model fit using the volume fractions and mean precipitate diameters in dependence of aging temperature gathered from the gradient aging experiment. We can rewrite Eq. (6) into the Arrhenius-like form in Eq. (7) using the relation $K(f_V) = K(0)\frac{27Y(f_V)}{4\bar{r}^3}$ [79], combining the coefficients into a single prefactor $A$, and introducing the activation energy for coarsening $E_A$.

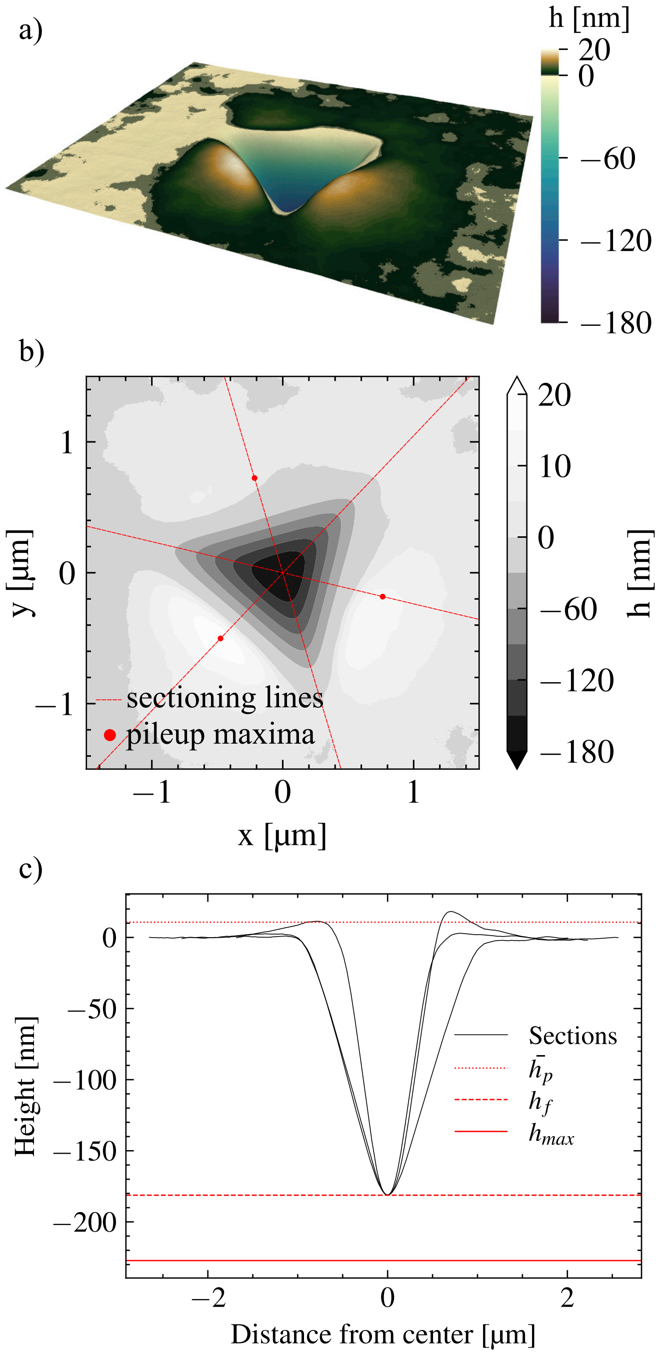

**Fig. 7.** Results of the pileup analysis for the indent located at aging temperature 647 °C shown in Fig. 6i. Indent topography is shown as a three-dimensional surface (a), a contour map (b) and in form of the sections used for pileup analysis (c). 3 lines are laid from the corners through the indent center to determine the pileup as the local maxima closest to the indent center. The determined maxima locations are shown in b), while the height profiles across the lines can be seen in c), which also shows the mean pileup height $h_p$ (dotted red), the final indent depth $h_f$ (dashed red) and the maximum indent depth $h_{max}$ (solid red). (For interpretation of the references to color in this figure legend, the reader is referred to the web version of this article.)

$$log(K(0)T) = log(A) - \frac{E_A}{R}\frac{1}{T} \tag{7}$$

From the fitted distributions in Fig. 10a, the actual mean three-dimensional precipitate diameters were extracted. Given an initial precipitate size $d_0 = 58$ nm after homogenization with water quenching, the rate constant $K(0)$ was calculated for each measured aging temperature. 95 % confidence intervals were calculated assuming systematic errors during imaging to be dominant. Focus, contrast, working distance and a large variety of other parameters, as well as environmental influences such as vibration, can cause a deviation on the order of a few image pixels width in the diameters determined by automatic image analysis, affecting all precipitates in the analyzed region. Assuming a standard deviation of 2 pixels width in the diameters obtained by automatic image analysis, we can calculate the confidence intervals shown in Fig. 11. Since the magnification was continually adjusted according to the apparent size of the precipitates, the resulting errors are roughly proportional to the measured diameters.

Fig. 11a shows the observed coarsening rate constants with the model fit. At low temperatures below 850 °C without significant coarsening, the measurement error largely dominates the value for the rate constants, at some points becoming negative as the measured mean diameters after aging $d$ are below the initial mean diameter $d_0$. The affected values were excluded for the linear regression. Fitting according to Eq. (7), we get the values $A = (8.18 \pm 2.51) \times 10^{-9}\,\mathrm{m^3\,s^{-1}\,K}$ and $E_A = 348 \pm 3$ kJ mol$^{-1}$, with the uncertainties calculated from the 95 % confidence intervals for the fitting parameters. The activation energy of coarsening thus determined is markedly higher than typically reported for Ni-based superalloys, which are mostly in the range 250–290 kJ mol$^{-1}$ (with singular values as high as 358 kJ mol$^{-1}$) [81,89]. However, similarly high values have been reported by Rieger et al. as 352 ± 29 kJ mol$^{-1}$ for $Al_{5.5}Ti_7Cr_{13.1}Fe_{8.8}Co_{25.2}Ni_{40.4}$ [90] and by Pandey et al. as 360 ± 50 kJ mol$^{-1}$ for $Co_{37.6}Ni_{35.4}Al_{9.9}Mo_{4.9}Cr_{5.9}Ta_{2.8}Ti_{3.5}$ [91]. As described in aforementioned work by Rieger et al., it is likely that the temperature-dependent composition difference between the $\gamma$ and $\gamma'$ phases increases the activation energy for coarsening, in addition to the activation energy for bulk diffusion.

Fig. 11b gives a comparison of the measured mean diameters with the results from the fitted model. In the LSEM model shown in red, precipitate coalescence leads to higher coarsening rates at lower temperatures/higher volume fractions. This is in good agreement with the experimental values, where there is a slightly decreased slope from the mostly linear, asymptotic part at higher temperatures to the left. Conversely, in the LSW model without dependence on volume fraction, there is a significant deviation from the observed values above 1100 °C, exceeding the upper confidence limit (see the magnified section in Fig. 11b). We thus assume that precipitate coalescence plays an essential part in the coarsening kinetics for the alloy TMP-5002. Traditional analyses using individually heat treated samples with significantly fewer data points over temperature have often been unable to experimentally reveal a significant influence of the volume fraction [89]. In comparison, the large amount of datapoints of the present high-throughput method experimentally reveals more subtle changes in the rate constant due to precipitate coalescence, which according to the LSEM theory are limited to a maximum factor of about 3 as compared to the LSW model [79].

### 4.2. Property: calculation of stress–strain curves

Using the data from Fig. 6 and Fig. 9, nanoindentation inverse analysis leads to the stress/strain curves presented in Fig. 12. Here, we assumed linear hardening behaviour, resulting in a constant slope in the plastic deformation regime. The only significant, discernable difference between the stress/strain curves is the yield strength, while the slopes of both the elastic and plastic regimes are highly similar. The key properties extracted from these curves are shown in Fig. 13, with yield strength and strain hardening rate plotted over a shared horizontal axis for the aging temperature. With the strain hardening coefficient $B$ being mostly independent of aging temperature (Fig. 13b), the yield strength (Fig. 13a) closely follows the measurement results for hardness (Fig. 9a), varying from approximately 600 MPa to 800 MPa. It needs to be assumed that the results for mechanical testing of macroscale samples will deviate from the values determined at the nanoscale, especially at

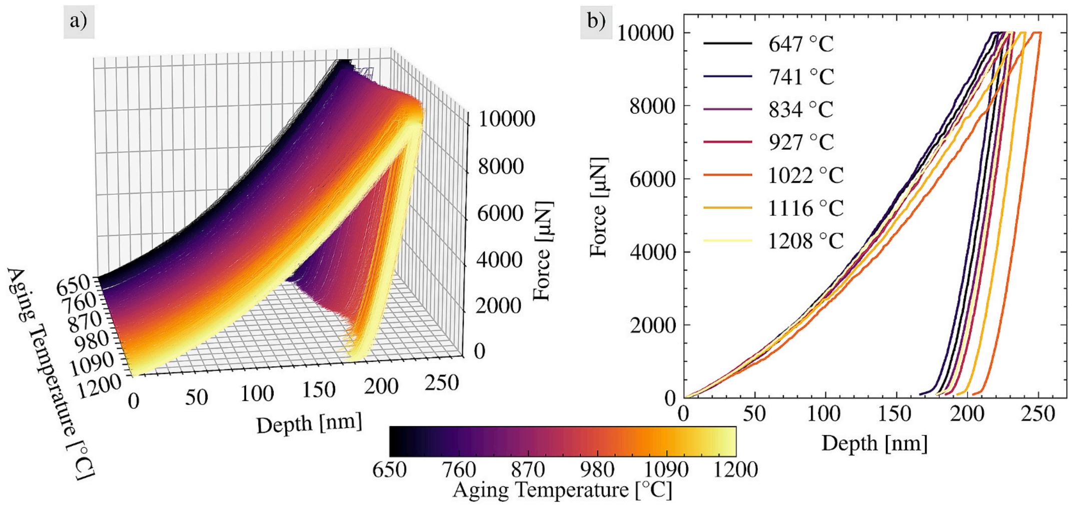

**Fig. 8.** Room temperature nanoindentation force/depth curves. a) All curves measured, b) Data for selected aging temperatures. Maximum load 10 mN, hold time 10 s, loading/unloading rate 2 mN/s.

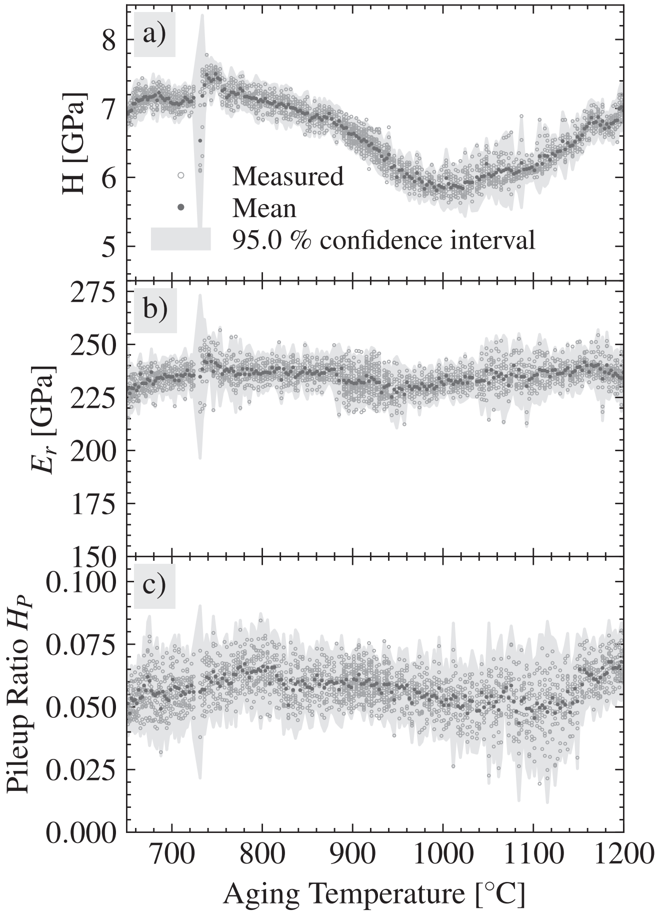

**Fig. 9.** Room temperature nanoindentation testing results. Hardness H (a), Reduced Youngs modulus $E_r$ (b) and the pileup ratio $H_p$ (c) determined from the four-channel AsB SEM images are given over a shared axis for the aging temperature.

the larger interparticle distances for the low volume fraction/large diameter regime above 1000 °C and below the solvus temperature.

### 4.3. Performance analysis of the high-throughput method

As a core metric for any high-throughput method, we will discuss the times necessary for sample preparation and measurements. A short graphical comparison is presented in Fig. 14, with the detailed times and estimates outlined below.

Preparation times are dominated by single crystal casting, effectively taking a full 24 h, and the homogenization treatment requiring 125 h for virtually complete elimination of segregation gradients. The aging treatment, including experimental setup and cleanup times, requires another 8 h, while polishing and machining times completed within 3 h of worktime, resulting in an overall preparation time of 160 h – or just short of one week of pure worktime – for the single crystal sample ready for analysis.

For the sample analysis, nanoindentation took a majority of the time required. Due to the required motor, piezo and drift settle times, a single indent required an average measurement time of 188 s, resulting in 125 h for all positions. SEM analysis was comparatively quicker with an average 44 s per position or 29 h overall for both the microstructure and indent pileup analysis routines. In total, analysis required 154 h of pure measurement time.

With measurement taking 154 h using the high-throughput single crystal sample prepared in 160 h, the overall time for the high-throughput method amounts to 314 h or just over 13 days. For the same amount of 2400 data points measured over the gradient sample, a more traditional analysis using tensile testing for the generation of stress/strain curves would require preparing 2400 tensile specimens. The calculations below assume using the same equipment as used for the sample in the present paper.

The casting dimensions allow for the creation of 16 tensile specimens from a single 24 h cast requiring, effectively requiring 1.5 h per specimens. Next, the 125 h homogenization could be performed in batches of 8 specimens per treatment cycle, coming to 15.6 h for each sample. Similarly, the 3 h aging treatment, with an additional 2 h heating time, could be performed with two batches of 5 specimens for each temperature (for a total of 10 at equal aging temperature as in the present paper), thus requiring 1 h each. Machining and testing of the tensile specimens is expected to take 8.4 h each based on a previous comparison by Goto et al. [84]. Therefore, generation of the same amount of stress/strain curves alone takes a total of 26.5 h each, or over 7 years and 3 months for all 2400 specimens, or approximately 200 times longer than

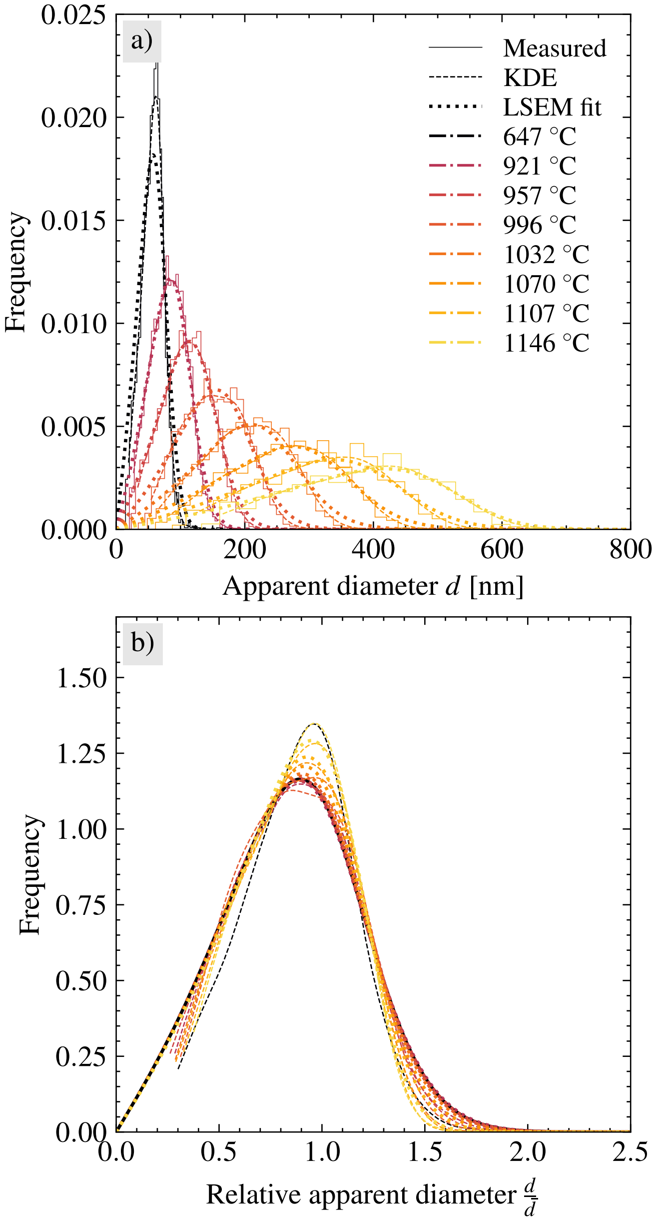

**Fig. 10.** SEM apparent precipitate size distributions fitted to measured distributions for selected temperatures. a) Absolute size distributions showing coarsening with temperature, b) Relative distributions by normalization using mean values, showing slight changes in distribution shape due to differing volume fractions.

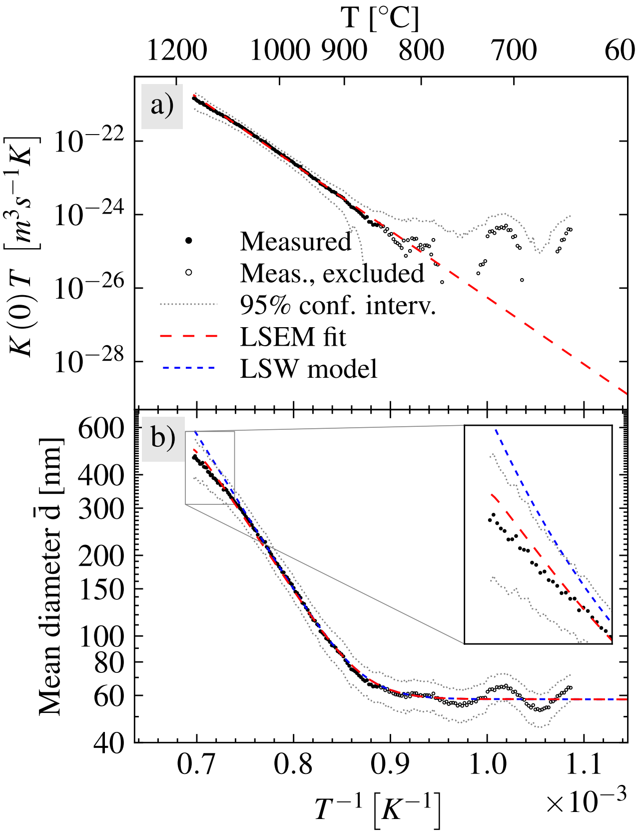

**Fig. 11.** LSEM coarsening fit (red, loosely dashed line) applied to the measured mean aging $\gamma'$ diameters (black circles), with comparison to the LSW model (blue, finely dashed line) without volume fraction dependence. Note that the confidence intervals shown are calculated assuming a systematic standard deviation of 2 pixels in the image analysis routine. (For interpretation of the references to color in this figure legend, the reader is referred to the web version of this article.)

the method proposed in this paper. One might argue that this is an excessive amount of data for the evaluation of the relatively simple sample presented in this paper, serving mainly as proof-of-concept for the high-throughput method. However, application of the method to more complex samples introducing additional degrees of freedom (composition, crystal orientation, etc.) would require an equal or even larger amount of measurements.

Microstructure analysis could then be performed from cutoff sections from tensile specimen machining, requiring no additional casting or heat treatment times. While polishing and imaging setup times for 220 samples to gather data at the same 220 temperatures would require additional time compared to the high-throughput method, the more pressing issue would be reproducibility of the polishing and imaging conditions. Further, imaging automation would be much more difficult, requiring constant operator attention, while the high-throughput sample could be comfortably setup to automatically image over a weekend, with no supervision required. Practically, imaging of 220 separate samples would be performed by multiple operators over weeks or months. Variations in imaging conditions and operator skill would further lead to degradation of data quality.

The method enables investigation of large composition and treatment temperature ranges, scanning for desirable as well as undesirable phases and improving assessments for phase diagrams, especially if combined with elemental analysis methods such as EPMA for measuring phase compositions. Composition data would further allow estimating interfacial energies as well as the effects of elemental partitioning varying with temperature on the activation energy for coarsening [90]. In combination with mechanical testing, relating the stress/strain response to the different material strengthening mechanisms could improve existing models, allowing prediction of the structure necessary for ideal properties. Besides physical models, the large amounts of data gatherable by the method would also make it well-suited for training models using machine learning in order to predict novel materials.

## 5. Conclusions

We have presented a high-throughput method allowing acquisition of 2400 sets of microstructure and mechanical property data for 220 different aging temperatures between 647 and 1208 °C. In an estimate, we calculated this method to be approximately 200 times faster than traditional testing using tensile specimens in order to acquire the same amount of stress/strain curves. While a more targeted analysis using

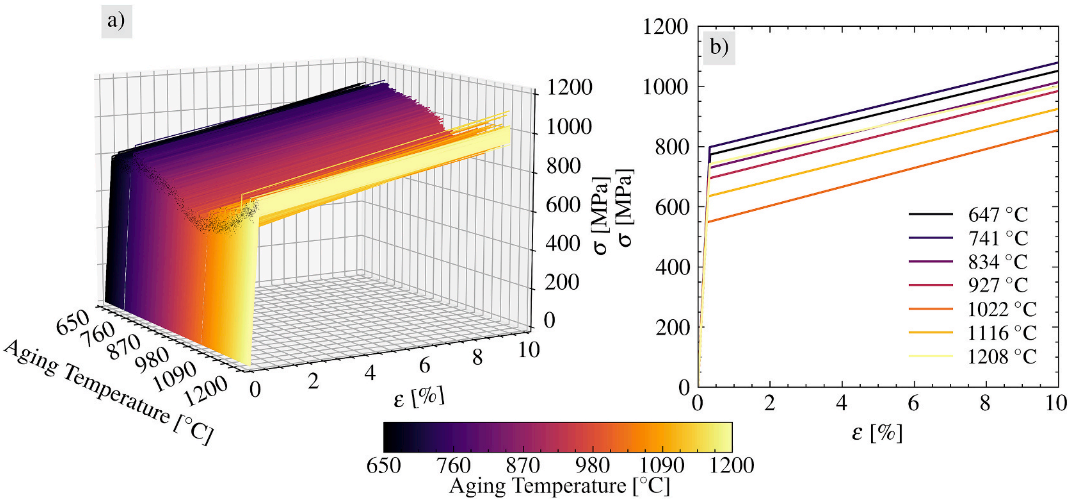

**Fig. 12.** Room temperature Stress/strain curves calculated by nanoindentation inverse analysis. a) Shows all temperatures evaluated with the yield points marked black, while b) shows select temperatures. Assuming linear hardening, the plastic flow regime has a constant slope equal to the strain hardening rate B.

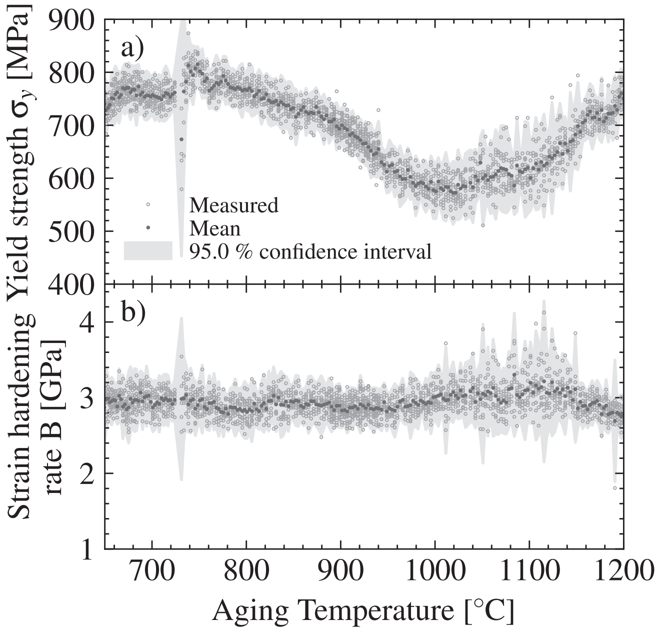

**Fig. 13.** Room temperature yield strength (a) and Strain hardening rate (b) over aging temperature, gathered as the slopes of the elastic and plastic deformation regimes of the stress/strain curves in Fig. 12, respectively.

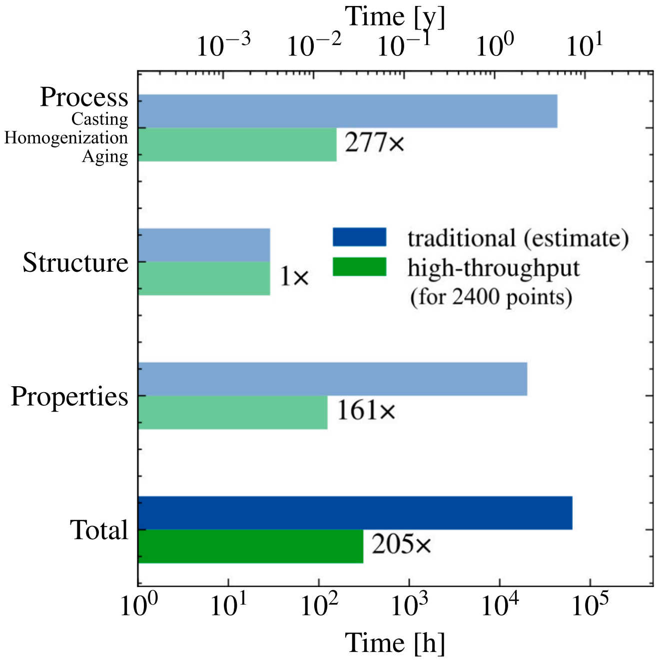

**Fig. 14.** Performance comparison between the high-throughput method presented here and an estimate for the same amount of data (2400 points) gathered by traditional methods. Times are given in a logarithmic scale for Process (casting, homogenization and aging), Structure (SEM imaging), Properties (nanoindentation and tensile testing) and in total, each with speedup factors of the high-throughput method compared to the traditional method. While negligible overall, SEM analysis for the traditional method was assumed to take the same 29 h as for the high-throughput method.

traditional methods could allow evaluating the mechanical properties of alloy TMP-5002 depending on aging treatment in a similar amount of time and cost as the high-throughput method, the large amounts of data gatherable by the high-throughput method allow comprehensive evaluation of more complex samples such as multi-diffusion couples [67] or similar multi-graded materials [62]. Beyond performance, this method also results in highly correlated and consistent data by performing all analyses on the same sample, aged in a continuous temperature gradient, at the same locations and in one measurement session, eliminating most environmental influences and variations due to different operators. While the relationship between hardness and yield strength for the alloy TMP-5002 used in the present paper was found to be mostly proportional due to the strain hardening rate determined from nanoindentation inverse analysis being mostly independent of aging temperature, coarsening rate analysis revealed a significant influence of the volume fraction present at aging temperature, owing to the high temperature resolution of the data measured. The data gathered in this work serves to optimize the heat treatment for tailoring volume fraction and size of the critically important secondary $\gamma'$ precipitates. Additional heat treatments of the gradient sample could further help optimization of tertiary $\gamma'$ for an optimal balance of mechanical properties.

In principle, the method presented here is applicable to any engineering material accessible to nanoindentation and SEM, featuring any type of gradient (e.g. concentration or deformation) or polycrystalline samples for investigating the effects of grain size or crystal orientation. Further, extending the method to include nanoindentation testing at high temperatures would aid gathering data particularly valuable for aerospace materials.

## CRediT authorship contribution statement

**Thomas Hoefler:** Writing – original draft, Visualization, Software, Investigation, Formal analysis. **Ayako Ikeda:** Investigation, Data curation. **Toshio Osada:** Writing – review & editing, Supervision, Project administration, Methodology, Conceptualization. **Toru Hara:** Methodology, Conceptualization. **Kyoko Kawagishi:** Resources. **Takahito Ohmura:** Writing – review & editing, Supervision, Project administration, Funding acquisition, Conceptualization.

## Declaration of competing interest

The authors declare the following financial interests/personal relationships which may be considered as potential competing interests: Financial support was provided by Acquisition Technology and Logistics Agency (ATLA), Tokyo/Japan. The authors have a patent pending to NIMS.

## Acknowledgements

This work was supported by the Innovative Science and Technology Initiative for Security of the Acquisition Technology and Logistics Agency (ATLA), Tokyo/Japan (Grant No. JPJ004596).

The authors would also like to extend their thanks to the following people at NIMS: Makoto Osawa for advice on experimental design, Yuji Takata for casting and evaluation of the single crystal samples, Takuma Kohata for providing guidance on SEM observations, Eri Nakagawa for offering counsel on nanoindentation testing, Koji Nakazato (Materials Forming Unit, MFU) for advice regarding metallographic preparation, Masahiko Kawasaki (MFU) for quartz encapsulation, and Kayoko Nakakita, Megumi Noro, Chieko Toku and Nana Fujibayashi for assisting sample preparation.

## Data availability

Data will be made available on request.

## References

[1] M. Cohen, Unknowables in the essence of materials science and engineering, Mater. Sci. Eng. 25 (1976) 3–4, https://doi.org/10.1016/0025-5416(76)90043-4.
[2] G.B. Olson, Computational design of hierarchically structured materials, Science 277 (5330) (1997) 1237–1242, https://doi.org/10.1126/science.277.5330.1237.
[3] W. Xiong, G.B. Olson, Cybermaterials: materials by design and accelerated insertion of materials, npj Comput, Mater 2 (1) (2016) 15009, https://doi.org/10.1038/npjcompumats.2015.9.
[4] D.L. McDowell, R.A. LeSar, The need for microstructure informatics in process-structure-property relations, , MRS Bulletin 41 (8) (2016) 587–593, https://doi.org/10.1557/mrs.2016.163.
[5] Materials Genome Initiative, URL: https://www.mgi.gov/ (visited on 11/11/2024).
[6] National Science and Technology Council, Materials Genome Initiative Strategic Plan, Nov. 2021, URL: https://www.mgi.gov/sites/mgi/files/MGI-2021-Strategic-Plan.pdf (visited on 11/06/2024).
[7] J.J. de Pablo, N.E. Jackson, M.A. Webb, et al., New frontiers for the materials genome initiative, npj Comput Mater 5 (2019) 41, https://doi.org/10.1038/s41524-019-0173-4.
[8] The European Materials Modelling Council, URL: https://emmc.eu/ (visited on 11/11/2024).
[9] N. Adamovic et al., European Materials Modelling Council, in: Proceedings of the 4th World Congress on Integrated Computational Materials Engineering (ICME2017), ed. by Paul Mason et al., Springer International Publishing, Cham, 2017 79–92.
[10] M. Demura, T. Koseki, SIP-materials integration projects, Mater. Trans. 61 (11) (2020) 2041–2046, https://doi.org/10.2320/matertrans.MT-MA2020003.
[11] L. Scotti, et al., Review of material modeling and digitalization in industry: barriers and perspectives, Integr. Mater. Manuf. Innov. 12 (4) (2023) 397–420, https://doi.org/10.1007/s40192-023-00318-2.
[12] L.K. Aagesen, et al., PRISMS: an integrated, open-source framework for accelerating predictive structural materials science, JOM 70 (10) (2018) 2298–2314, https://doi.org/10.1007/s11837-018-3079-6.
[13] Center for Hierarchical Materials Design, URL: https://chimad.northwestern.edu/ (visited on 11/15/2024).
[14] Interdisciplinary Centre for Advanced Materials Simulation, URL: https://www.icams.de/ (visited on 11/11/2024).
[15] M. Demura, Materials integration for accelerating research and development of structural materials, Mater. Trans. 62 (11) (2021) 1669–1672, https://doi.org/10.2320/matertrans.MT-M2021135.
[16] QuesTek Innovations LLC, URL: https://questek.com/ (visited on 11/11/2024).
[17] H. Springer, D. Raabe, Rapid alloy prototyping: Compositional and thermomechanical high throughput bulk combinatorial design of structural materials based on the example of 30Mn–1.2C–xAl triplex steels, Acta Materialia 60 (12) (2012) 4950–4959, https://doi.org/10.1016/j.actamat.2012.05.017.
[18] T.L. Burnett, P.J. Withers, Completing the picture through correlative characterization, Nat. Mater. 18 (10) (2019) 1041–1049, https://doi.org/10.1038/s41563-019-0402-8.
[19] W. Betteridge, S.W.K. Shaw, Development of superalloys, Mater. Sci. Technol. 3 (9) (1987) 682–694, https://doi.org/10.1179/mst.1987.3.9.682.
[20] C.T. Sims, N.S. Stoloff, W.C. Hagel, Superalloys II, Wiley-Interscience, New York, NY, 1987.
[21] R.C. Reed, The Superalloys: Fundamentals and Applications, Cambridge University Press, 2008.
[22] H. Harada, H. Murakami, Design of Ni-Base Superalloys, in: Tetsuya Saito (Ed.), Computational Materials Design, Springer Berlin Heidelberg, Berlin, Heidelberg, 1999, pp. 39–70, https://doi.org/10.1007/978-3-662-03923-6_2.
[23] J.-W. Yeh, et al., Nanostructured high-entropy alloys with multiple principal elements: novel alloy design concepts and outcomes, Adv. Eng. Mater. 6 (5) (2004) 299–303, https://doi.org/10.1002/adem.200300567.
[24] B. Cantor, et al., Microstructural development in equiatomic multicomponent alloys, Mater. Sci. Eng. A 375–377 (2004) 213–218, https://doi.org/10.1016/j.msea.2003.10.257.
[25] E.P. George, D. Raabe, R.O. Ritchie, High-entropy alloys, Nat. Rev. Mater. 4 (8) (2019) 515–534, https://doi.org/10.1038/s41578-019-0121-4.
[26] Y.F. Ye, et al., High-entropy alloy: challenges and prospects, Mater. Today 19 (6) (2016) 349–362, https://doi.org/10.1016/j.mattod.2015.11.026.
[27] D.B. Miracle, O.N. Senkov, A critical review of high entropy alloys and related concepts, Acta Mater. 122 (2017) 448–511, https://doi.org/10.1016/j.actamat.2016.08.081.
[28] G.R. Weber, S. Ghosh, Thermo-mechanical deformation evolution in polycrystalline Ni-based superalloys by a hierarchical crystal plasticity model, Mater. High Temp. 33 (4–5) (2016) 401–411, https://doi.org/10.1080/09603409.2016.1190147.
[29] J. Ruzic, et al., Temperature-dependent deformation behavior of $\gamma$ and $\gamma'$ single-phase nickel-based superalloys, Mater. Sci. Eng. A 818 (2021) 141439, https://doi.org/10.1016/j.msea.2021.141439.
[30] M. Durand-Charre, The Microstructure of Superalloys, Routledge, 2017.
[31] A.J. Goodfellow, et al., Gamma prime precipitate evolution during aging of a model nickel-based superalloy, Metall. Mater. Trans. A 49 (3) (2018) 718–728, https://doi.org/10.1007/s11661-017-4336-y.
[32] D.J. Sauza, et al., $\gamma'$-(L12) precipitate evolution during isothermal aging of a CoAlWNi superalloy, Acta Mater. 164 (2019) 654–662, https://doi.org/10.1016/j.actamat.2018.11.014.
[33] P.J. Bocchini, et al., Temporal evolution of a model Co-Al-W superalloy aged at 650 °C and 750 °C, Acta Mater. 159 (2018) 197–208, https://doi.org/10.1016/j.actamat.2018.08.014.
[34] P. Zhang, et al., Morphological evolution of $\gamma'$ precipitates in superalloy M4706 during thermal aging, Mater. Lett. 211 (2018) 107–109, https://doi.org/10.1016/j.matlet.2017.09.096.
[35] S. Meher, et al., Coarsening kinetics of $\gamma'$ precipitates in cobalt-base alloys, Acta Mater. 61 (11) (2013) 4266–4276, https://doi.org/10.1016/j.actamat.2013.03.052.
[36] V. Nandal, et al., Artificial intelligence inspired design of non-isothermal aging for $\gamma$- $\gamma'$ two-phase, Ni-Al alloys, Sci. Rep. 13 (1) (2023) 12660, https://doi.org/10.1038/s41598-023-39589-2.
[37] M.C. Hardy, et al., Solving recent challenges for wrought Ni-base superalloys, Metall. Mater. Trans. A 51 (6) (2020) 2626–2650, https://doi.org/10.1007/s11661-020-05773-6.
[38] H. Harada, et al., Phase calculation and its use in alloy design program for nickel-base superalloys, Superalloys 1988 (1988) 733–742.
[39] T. Yokokawa, et al., Advanced alloy design program and improvement of sixth-generation ni-base single crystal superalloy TMS-238, in: S. Tin (Ed.), Superalloys 2020, Springer International Publishing, Cham, 2020, pp. 122–130.
[40] A.-C. Yeh, et al., On the creep and phase stability of advanced Ni-base single crystal superalloys, Mater. Sci. Eng. A 490 (1) (2008) 445–451, https://doi.org/10.1016/j.msea.2008.02.008.
[41] N. Saunders et al., Phase diagram calculations for Ni-based superalloys, in: Superalloys 1996, ed. by R. D. Kissinger et al, The Minerals, Metals & Materials Society, 1996.
[42] N. Dupin, B. Sundman, A thermodynamic database for Ni-base superalloys, Scand. J. Metall. 30 (3) (2001) 184–192, https://doi.org/10.1034/j.1600-0692.2001.300309.x.
[43] C.E. Campbell, W.J. Boettinger, U.R. Kattner, Development of a diffusion mobility database for Ni-base superalloys, Acta Mater. 50 (4) (2002) 775–792, https://doi.org/10.1016/S1359-6454(01)00383-4.

[44] H. Lukas, S.G. Fries, B.o. Sundman, C. Thermodynamics, The Calphad Method, 1st, Cambridge University Press, USA, 2007.

[45] C.E. Campbell, U.R. Kattner, Z.-K. Liu, The development of phase based property data using the CALPHAD method and infrastructure needs, Integr. Mater. Manuf. Innov. 3 (1) (2014) 158–180, https://doi.org/10.1186/2193-9772-3-12.

[46] C.E. Campbell, U.R. Kattner, Z.-K. Liu, File and data repositories for next generation CALPHAD, Scr. Mater. 70 (2014) 7–11, https://doi.org/10.1016/j.scriptamat.2013.06.013.

[47] Z.-K. Liu, First-principles calculations and CALPHAD modeling of thermodynamics, J. Phase Equilib. Diffus. 30 (5) (2009) 517–534, https://doi.org/10.1007/s11669-009-9570-6.

[48] Z.-K. Liu, Thermodynamics and its prediction and CALPHAD modeling: Review, state of the art, and perspectives, Calphad 82 (2023) 102580, https://doi.org/10.1016/j.calphad.2023.102580.

[49] D.J. Crudden, et al., Modelling of the influence of alloy composition on flow stress in high-strength nickel-based superalloys, Acta Mater. 75 (2014) 356–370, https://doi.org/10.1016/j.actamat.2014.04.075.

[50] T.M. Smith, et al., Phase transformation strengthening of high-temperature superalloys, Nat. Commun. 7 (1) (2016) 13434, https://doi.org/10.1038/ncomms13434.

[51] G.L.W. Hart, et al., Machine learning for alloys, Nat. Rev. Mater. 6 (8) (2021) 730–755, https://doi.org/10.1038/s41578-021-00340-w.

[52] P. Liu, et al., Machine learning assisted design of $\gamma'$-strengthened Co-base superalloys with multi-performance optimization, npj Comput. Mater. 6 (1) (2020) 62, https://doi.org/10.1038/s41524-020-0334-5.

[53] L. Montanelli, et al., High-throughput extraction of phase-property relationships from literature using natural language processing and large language models, Integr. Mater. Manuf. Innov. 13 (2) (2024) 396–405, https://doi.org/10.1007/s40192-024-00344-8.

[54] M.J. Buehler, MechGPT, a language-based strategy for mechanics and materials modeling that connects knowledge across scales, disciplines, and modalities, Appl. Mech. Rev. 76 (2) (Jan. 2024) 021001, https://doi.org/10.1115/1.4063843.

[55] A.R. Durmaz, et al., An ontology-based text mining dataset for extraction of process-structure-property entities, Sci. Data 11 (1) (2024) 1112, https://doi.org/10.1038/s41597-024-03926-5.

[56] T. Gupta, et al., MatSciBERT: A materials domain language model for text mining and information extraction, npj Comput. Mater. 8 (1) (2022) 102, https://doi.org/10.1038/s41524-022-00784-w.

[57] J. Dagdelen, et al., Structured information extraction from scientific text with large language models, Nat. Commun. 15 (1) (2024) 1418, https://doi.org/10.1038/s41467-024-45563-x.

[58] W. Wang, et al., Automated pipeline for superalloy data by text mining, npj Comput Mater. 8 (1) (2022) 9, https://doi.org/10.1038/s41524-021-00687-2.

[59] Z. Qin, et al., Phase prediction of Ni-base superalloys via high-throughput experiments and machine learning, Mater. Res. Lett. 9 (1) (2021) 32–40, https://doi.org/10.1080/21663831.2020.1815093.

[60] Z.i. Wang, et al., A high-throughput approach to explore the multi-component alloy space: a case study of nickel-based superalloys, J. Alloy. Compd. 858 (2021) 158100, https://doi.org/10.1016/j.jallcom.2020.158100.

[61] W. Li, et al., High-throughput exploration of alloying effects on the microstructural stability and properties of multi-component CoNi-base superalloys, J. Alloy. Compd. 881 (2021) 160618, https://doi.org/10.1016/j.jallcom.2021.160618.

[62] A. Ikeda, et al., High-throughput mapping method for mechanical properties, oxidation resistance, and phase stability in Ni-based superalloys using composition-graded unidirectional solidified alloys, Scr. Mater. 193 (2021) 91–96, https://doi.org/10.1016/j.scriptamat.2020.10.043.

[63] F. Liu, et al., High-throughput method–accelerated design of Ni-based superalloys, Adv. Funct. Mater. 32 (28) (2022) 2109367, https://doi.org/10.1002/adfm.202109367.

[64] P. Liu, et al., Evolution analysis of $\gamma'$ precipitate coarsening in Co-based superalloys using kinetic theory and machine learning, Acta Mater. 235 (2022) 118101, https://doi.org/10.1016/j.actamat.2022.118101.

[65] S. Lech, et al., Evolution of microstructure and mechanical properties of ATI 718Pluso superalloy after graded solution treatment, Metall. Mater. Trans. A 54 (5) (2023) 2011–2021, https://doi.org/10.1007/s11661-022-06859-z.

[66] S. Chen, et al., High-throughput screening of multicomponent alloy compositions with optimal mechanical properties using two-step diffusion multiple: Demo in Al–Co–Cr–Fe–Ni–Ti high-entropy superalloys, Mater. Sci. Eng. A 910 (2024) 146909, https://doi.org/10.1016/j.msea.2024.146909.

[67] K. Goto, et al., High-throughput evaluation of stress–strain relationships in Ni–Co–Cr ternary systems via indentation testing of diffusion couples, J. Alloy. Compd. 910 (2022) 164868, https://doi.org/10.1016/j.jallcom.2022.164868.

[68] S. Medghalchi, et al., Automated segmentation of large image datasets using artificial intelligence for microstructure characterisation and damage analysis, Mater. Des. 243 (2024) 113031, https://doi.org/10.1016/j.matdes.2024.113031.

[69] Y.F. Gu, T. Osada, T. Yokokawa, H. Harada, J. Fujioka, D. Nagahama, M. Okuno. Development of Nickel-Cobalt Base P/M Superalloys for Disk Applications, Superalloys, 2016, https://doi.org/10.1002/9781119075646.ch23.

[70] R. Yurishima, et al., Microstructure optimization of thermoelectric $\tau 1 - Al_2Fe_3Si_3$ via graded temperature heat treatments, Materials 17 (23) (2024), https://doi.org/10.3390/ma17235899.

[71] G. Bradski, The OpenCV Library, Dr. Dobb's Journal of Software Tools (2000).

[72] S. van der Walt, et al., scikit-image: image processing in Python, PeerJ 2 (2014) e453.

[73] Eric W. Weisstein, Superellipse, July 2024, URL: https://mathworld.wolfram.com/Superellipse.html (visited on 08/06/2024).

[74] S.A. Saltykov, Stereometric Metallography, 267, Metallurgizdat, Moscow, 1958.

[75] D. Michael, Higgins, measurement of crystal size distributions, Am. Mineral. 85 (9) (Sept. 2000) 1105–1116, https://doi.org/10.2138/am-2000-8-901.

[76] E.J. Payton, Revisiting sphere unfolding relationships for the stereological analysis of segmented digital microstructure images, J. Miner. Mater. Charact. Eng. 11 (03) (2012) 22, https://doi.org/10.4236/jmmce.2012.113018.

[77] J. Takahashi, H. Suito, Evaluation of the accuracy of the three-dimensional size distribution estimated from the schwartz-saltykov method, Metall. Mater. Trans. A 34 (1) (2003) 171–181, https://doi.org/10.1007/s11661-003-0218-6.

[78] J. Takahashi, H. Suito, Random dispersion model of two-dimensional size distribution of second-phase particles, Acta Mater. 49 (4) (2001) 711–719, https://doi.org/10.1016/S1359-6454(00)00350-5.

[79] C.K.L. Davies, P. Nash, R.N. Stevens, The effect of volume fraction of precipitate on Ostwald ripening, Acta Metall. 28 (2) (1980) 179–189, https://doi.org/10.1016/0001-6160(80)90067-X.

[80] A. Baldan, Review Progress in Ostwald ripening theories and their applications to nickel-base superalloys Part I: Ostwald ripening theories, J. Mater. Sci. 37 (11) (2002) 2171–2202, https://doi.org/10.1023/A:1015388912729.

[81] A. Baldan, Review progress in Ostwald ripening theories and their applications to the $\gamma'$-precipitates in nickel-base superalloys Part II Nickel-base superalloys, J. Mater. Sci. 37 (12) (2002) 2379–2405, https://doi.org/10.1023/A:1015408116016.

[82] I.M. Lifshitz, V.V. Slyozov, The kinetics of precipitation from supersaturated solid solutions, J. Phys. Chem. Solid 19 (1) (1961) 35–50, https://doi.org/10.1016/0022-3697(61)90054-3.

[83] K. Goto, I. Watanabe, T. Ohmura, Determining suitable parameters for inverse estimation of plastic properties based on indentation marks, Int. J. Plast 116 (2019) 81–90, https://doi.org/10.1016/j.ijplas.2018.12.007.

[84] K. Goto, I. Watanabe, T. Ohmura, Inverse estimation approach for elastoplastic properties using the load-displacement curve and pile-up topography of a single Berkovich indentation, Mater. Des. 194 (2020) 108925, https://doi.org/10.1016/j.matdes.2020.108925.

[85] S.S. Babu, et al., Characterization of the microstructure evolution in a nickel base superalloy during continuous cooling conditions, Acta Mater. 49 (20) (2001) 4149–4160, https://doi.org/10.1016/S1359-6454(01)00314-7.

[86] P. Li, et al., Effect of cooling rate on the Morphological changes in the secondary $\gamma'$ precipitation in FGH97 nickel-based PM superalloy, Intermetallics 171 (2024) 108344, https://doi.org/10.1016/j.intermet.2024.108344.

[87] W. Yang, et al., The effect of Fe addition on $\gamma'$ precipitates during thermal exposure in Ni-Co-based single crystal superalloys, J. Mater. Res. Technol. 20 (2022) 894–904, https://doi.org/10.1016/j.jmrt.2022.07.135.

[88] R. Radis, et al., Multimodal size distributions of $\gamma'$ precipitates during continuous cooling of UDIMET 720 Li, Acta Mater. 57 (19) (2009) 5739–5747, https://doi.org/10.1016/j.actamat.2009.08.002.

[89] D.J. Chellman, A.J. Ardell, The coarsening of $\gamma'$ precipitates at large volume fractions, Acta Metall. 22 (5) (1974) 577–588, https://doi.org/10.1016/0001-6160(74)90155-2.

[90] T. Rieger, et al., Influence of chemical composition on coarsening kinetics of coherent L12 precipitates in FCC complex concentrated alloys, J. Alloy. Compd. 967 (2023) 171711, https://doi.org/10.1016/j.jallcom.2023.171711.

[91] P. Pandey, et al., On the high temperature coarsening kinetics of $\gamma'$ precipitates in a high strength Co37.6Ni35.4Al9.9Mo4.9Cr5.9Ta2.8Ti3.5 fcc-based high entropy alloy, Acta Mater. 177 (2019) 82–95, https://doi.org/10.1016/j.actamat.2019.07.011.